MeV Electron Precipitation during Radiation Belt Dropouts

Domenique Freund[1], Lauren Blum[1], Sergio Vidal-Luengo[1], Alessandro Bruno[2,3] Ryuho Kataoka[4]

[1]Laboratory for Atmospheric and Space Physics, Boulder, Colorado, USA
[2]Heliophysics Science Division, NASA Goddard Space Flight Center, Greenbelt, MD, USA
[3]Department of Physics, Catholic University of America, Washington, DC, USA
[4]National Institute of Polar Research, Tachikawa-city, Tokyo, Japan

Key Points:

- MeV electron dropouts with and without associated precipitation show dependencies on solar cycle and seasons.
- An increase in precipitation occurrence and intensity during MeV dropouts aligns with the decline in SYM-H and B_z, and the peak in P_{dyn}.
- Dropouts with MeV electron precipitation, on average, spread over a wider radial extent, with occurrences related to SYM-H.

Corresponding author: Domenique Freund, `domenique.freund@lasp.colorado.edu`

Abstract

To gain deeper insights into radiation belt loss into the atmosphere, a statistical study of MeV electron precipitation during radiation belt dropout events is undertaken. During these events, electron intensities often drop by an order of magnitude or more within just a few hours. For this study, dropouts are defined as a decrease by at least a factor of 5 in less than 8 hours. Van Allen probe measurements are employed to identify dropouts across various parameters, complemented by precipitation data from the CALorimetric Electron Telescope instrument on the International Space Station. A temporal analysis unveils a notable increase in precipitation occurrence and intensity during dropout onset, correlating with the decline of SYM-H, the north-south component of the interplanetary magnetic field, and the peak of the solar wind dynamic pressure. Moreover, dropout occurrences show correlations with the solar cycle, exhibiting maxima at the spring and autumn equinoxes. This increase during equinoxes reflects the correlation between equinoxes and the SYM-H index, which itself exhibits a correlation with precipitation during dropouts. Spatial analysis reveals that dropouts with precipitation penetrate into lower L-star regions, mostly reaching L-star < 4, while most dropouts without precipitation don't penetrate deeper than L-star 5. This is consistent with the larger average dimensions of dropouts associated with precipitation. During dropouts, precipitation is predominantly observed in the dusk-midnight sector, coinciding with the most intense precipitation events. The results of this study provide insight into the contribution of precipitation to radiation belt dropouts by deciphering when and where precipitation occurred.

Plain Language Summary

The outer radiation belt encircles Earth, trapping energetic electrons due to the planet's magnetic field. Under certain conditions, such as during geomagnetic storms, there can be a significant loss of these trapped electrons over a short period, known as a dropout. One reason for this can be particles reentering Earth's atmosphere, leading to their removal from the outer radiation belt. This is referred to as precipitation. This study investigates the role of precipitation for dropouts, focusing on when and where precipitation occurs during those events. To accomplish this, data from the Van Allen Probe spacecraft, measuring electron density, and the CALorimetric Electron Telescope instrument aboard the International Space Station, measuring precipitation, are utilized. The findings reveal a correlation between dropouts, whether aligned with precipitation or not, and the solar cycle and seasons. Seasonal variations are likely connected to the intensity of disturbances in the magnetosphere, consequently raising the probability of precipitation. Spatial investigations reveal that dropouts accompanied by precipitation penetrate deeper into lower regions of stably trapped particles. Furthermore, precipitation predominantly occurs on the dusk and midnight side of Earth, where the strongest precipitation measurements are also recorded.

1 Introduction

The inner magnetosphere is comprised of torus-like regions encircling Earth, known as radiation belts, within which charged particles are trapped along Earth's magnetic field lines. This domain is divided by the slot region into two components: the inner radiation belt ($L \sim 1 - 2$) and the outer radiation belt ($L \sim 3 - 8$) (Van Allen, 1959). Energetic protons dominate the relatively stable inner radiation belt, while the dynamic outer radiation belt consists of energetic electrons spanning tens of keV to several MeV.

The unpredictable variability of the outer belt primarily stems from solar activity and subsequent geomagnetic disturbances. These disturbances drive a complex interplay of competing acceleration and loss mechanisms. Those loss mechanisms include magnetopause shadowing, outward radial diffusion, and wave-particle interactions, ultimately leading to the precipitation of particles into the Earth's atmosphere (Millan & Thorne, 2007; Moya et al., 2017; Turner, Morley, et al., 2012; Shprits et al., 2008; Loto'aniu et al., 2010; Green & Kivelson, 2004). Some of the most pronounced changes within Earth's outer radiation belt manifest as dropouts, which denote substantial depletions of the outer radiation belt, frequently witnessed during the main phase of geomagnetic storms (Baker et al., 1994; Xiang et al., 2018). These occurrences are characterized by a drastic reduction in electron flux across a wide spectrum of energies and spatial domains, occurring within a span of just a few hours (Friedel et al., 2002; Turner, Morley, et al., 2012).

In the case of dropout events, the combined effects of magnetopause shadowing and outward radial diffusion have been identified as significant contributors. However, these processes often fail to fully explain the observed depletion, necessitating the inclusion of an additional loss mechanism in the form of artificial "fast scattering" in simulations, particularly to replicate depletions at lower L shells ($L \lesssim 4$) (Shprits et al., 2006; Turner, Shprits, et al., 2012). "Fast scattering" encompasses pitch angle scattering of relativistic electrons, leading to Relativistic Electron Precipitation (REP). In high L-star regions, a combination of magnetopause shadowing, outward radial diffusion and particle scattering is expected to contribute to dropout events, while in low L-star regions, particle precipitation is suggested to be the primary driver (Xiang et al., 2018).

Pitch angle scattering can occur through two distinct mechanisms, either separately or in combination (Horne et al., 2009; Capannolo et al., 2022). The first process involves wave-particle interaction, which entails the exchange of energy and momentum between electromagnetic waves and charged particles. Different types of waves cause pitch angle scattering across various energy ranges. With a focus on MeV precipitation in this study, waves that influence precipitation within the MeV range are of particular interest as they could potentially act as drivers. Electro Magnetic Ion Cyclotron (EMIC) waves have been proposed as generators of REP events in the MeV range, particularly affecting particles with low pitch angles (Millan & Thorne, 2007; Summers & Thorne, 2003; Xiang et al., 2017, 2018). Scattering attributed to EMIC waves is anticipated to occur predominantly in the sectors from dawn to dusk (Allen et al., 2015), but is inadequate to explain the observed loss in the MeV energy range. Therefore, the inclusion of Hiss and whistler mode chorus waves is necessary (Drozdov et al., 2020).

The second mechanism for pitch angle scattering is current sheet scattering (CSS), which occurs when the Earth's magnetic field curvature radius approaches the gyroradius of electrons, violating the first adiabatic invariant. This phenomenon is associated with increased stretching of magnetic field lines and predominantly occurs in the nightside magnetosphere where the current sheet thins. Unlike wave-driven REP, which can be observed within the plasmasphere, CSS-driven REP is preferentially detected outside of it (Büchner & Zelenyi, 1989; Capannolo et al., 2022).

The relative importance of precipitation compared to other loss mechanisms such as magnetopause shadowing and outward radial diffusion remains incompletely understood but appears to depend on energy, L-star, and disturbance conditions. Yu et al. (2013) found for 649 keV electrons that losses for L-star > 5 are predominantly due to magnetopause shadowing and outward radial diffusion, whereas for L-star < 5, these mechanisms explain only 60% of losses. Reeves et al. (2003) observed significant losses for 1.8-3.5 MeV electrons at low L-shells, even when the magnetopause was far outwards, suggesting precipitation maybe a prevalent loss mechanism. Additionally, Xiong et al. (2015) demonstrated through superposed epoch analyses that storms with 'energy-dependent' responses enhance the likelihood of precipitation as an important loss process. Meanwhile, Gokani et al. (2019) studied precipitation during the 2015 Saint Patrick's Day storm and found it contributed less than 0.5% to the total loss of 0.9-6.3 MeV electrons.

While MeV precipitation is commonly suggested as a loss mechanism during fast depletions, there is still limited direct observational evidence to confirm that MeV electron precipitation actually contributes to dropouts (Bruno et al., 2022; Blum et al., 2024). Furthermore, our understanding of where and when precipitation can occur, as well as the relative importance of precipitation loss compared to other loss mechanisms such as outer boundary loss, remains incomplete. The significant importance of understanding precipitation events lies in the potential consequences of these events. REP events not only contribute to atmospheric heating but also pose risks to astronaut health during spacewalks and can lead to spacecraft anomalies (Goldberg et al., 1995; Dachev, 2018). Furthermore, studying MeV precipitation during dropout events contributes to a broader understanding of the outlined precipitation drivers.

This statistical study investigates the temporal and spatial occurrence of MeV electron precipitation during dropout events over a span of four years to enhance the overall comprehension of dropout events.

2 Data and Methodology

2.1 Datasets

To identify dropout events, electron fluxes from the Van Allen Probes are analyzed. The twin Van Allen Probes operated from 2012 to 2019 in a highly elliptical near-equatorial orbit, with a period of ∼9 hours and an apogee of ∼5.8 R_E, inside geostationary orbit (Mauk et al., 2013). This analysis involves utilizing a merged dataset from the Magnetic Electron Ion Spectrometer (MagEIS) (Blake et al., 2013) and the Relativistic Electron Proton Telescope (REPT) (Baker et al., 2013) onboard the Van Allen Probes. MagEIS captured radiation belt electron data from ∼200, keV to ∼3, MeV, while REPT measured electrons ranging from ∼1.6, MeV to ∼19, MeV. To resolve an offset in the overlapping channels of the two datasets, a spline fitting technique was employed by Boyd et al. (2021) to merge the data. This study utilizes the Magnetic Ephemeris data from the Van Allen Probes, calculated using the Tsyganenko and Sitnov 2004 (TS04) magnetic field model.

To identify MeV precipitation events, measurements from the CALorimetric Electron Telescope (CALET) are employed. Data collection by CALET commenced in August 2015 (Torii et al., 2019). The instrument flies onboard the International Space Station (ISS), maintaining a low Earth orbit at altitudes ranging from 370 to 460 km and an inclination of 51.6°. It measures the lower altitude footprints of the outer radiation belt, which can be mapped to L-shells 3-7 and is sampled multiple times daily across various magnetic local time (MLT) locations. CALET has a charge detector equipped with two scintillator arrays, CHDX and CHDY, adept at detecting electrons with energies surpassing 1.5 MeV and 3.4 MeV, respectively (Bruno et al., 2022). Rapid electron precipitation events measured by CALET are discernible through isolated surges in count rates (Kataoka et al., 2016, 2020). A catalogue of REP events observed by CALET, identified through a self-organizing map technique, is employed in this study (Vidal-Luengo et al., 2024). Specifically, the detected electron enhancements have been subdivided into two main categories: 1) rapid profiles, characterized by sharp temporal variations that can last from a few seconds to several minutes; and 2) smooth profiles, exhibiting a gradual increase followed by a decrease in count rates, typically spanning 5–10 minutes. Only the first event class is taken into account in this analysis, since smooth profiles are typically due to drift loss cone precipitation, and therefore cannot be precisely associated with certain dropout events in time and location. The overlapping time period between CALET and the Van Allen Probes used in this paper's analysis covers the period from the beginning of November 2015 to the end of June 2019.

In addition to radiation belt electron data, solar wind data and geomagnetic indices (OMNI) are employed to enhance our comprehension of the background conditions during dropout and precipitation events.

2.2 Methodology

To quantitatively assess radiation belt changes, identifying irreversible, non-adiabatic alterations is crucial, signifying genuine enhancements or depletions. The adiabatic invariants

$$\mu = \frac{p_\perp^2}{2m_0B} = \frac{p^2 sin^2\alpha}{2m_0B}$$

$$K = \frac{J}{2\sqrt{2m_0\mu}} = \int_{s'_m}^{s_m} \sqrt{B_m - B_s}ds$$

$$L^* = \frac{2\pi M}{|\Phi| R_E}$$

are used to reveal particle kinematics within the geomagnetic field (Green & Kivelson, 2004; Roederer & Zhang, 2014). The first invariant, denoted as μ, represents the magnetic moment, illustrating the trajectory of particles as they gyrate along magnetic field lines. Here, $p_\perp$ signifies the component of relativistic momentum perpendicular to the magnetic field, m_0 denotes the rest mass of the electron, B stands for the magnitude of the magnetic field, and α represents the pitch angle. The second invariant, conventionally expressed as K, correlates with bounce motion. J represents the longitudinal invariant, while s_m and s'_m indicate the distances from the particle's mirror point, where the particle undergoes bouncing. B_s and B_m signify the magnetic field magnitudes at points s and the mirror point, respectively. The third invariant, symbolized as L-star (L^*), embodies a property of stably trapped particles and conveniently relates inversely proportional to the magnetic flux Φ. Here, M represents the magnetic moment of Earth's dipole field, and R_E denotes the radius of the Earth.

For this study, the adiabatic invariants are used to compute the PSD from electron flux data measured by the Van Allen Probes, representing particle concentration in the combined space of position and momentum. Utilizing a 4-hour time resolution, the measurements are aggregated into 4-hour intervals, and data gaps along the L-star parameter are interpolated. To identify dropout events, the procedure utilized by Xiang et al. (2018) is employed, where a decrease in PSD exceeding a factor of five within a span of less than eight hours is classified as a dropout event. In this study, the commencement of a dropout is defined as the time step where the PSD first decreases by a factor of at least five, while the end of a dropout is defined as the time step where the PSD is no longer decreasing.

A catalog is compiled for the specified data timeframe, detailing the PSD for given K and μ values across L-star. An example page of the catalogue is illustrated in Figure 1. The white dotted line denotes storms identified by Turner et al. (2019), while diamonds represent all REP events identified from the measurements of CALET, with color indicating their intensity in counts. The pink circles in the lower plot highlight identified dropouts. Additionally, the figure is overlaid with the SYM-H index.

If multiple dropout events are detected within a 2-day timeframe, they are considered a single event independent of their L-star region. This approach prevents inadvertent categorization into separate dropout events due to missing data points or variations in loss processes over different timescales. Throughout the investigated timeframe, no instances occurred where different storm events associated with a dropout happened closer together than 2 days, ensuring accurate identification of distinct events. Figure 1 serves as an example where the detected dropouts, indicated by pink circles, are counted as three distinct dropout events. Moreover, the calculation of the last closed drift shell (LCDS) helps determine whether magnetopause shadowing, rather than precipitation, was the predominant influencing factor. Pinto et al. (2020), shows that electron outward radial diffusion driven by intense ULF waves, along with magnetopause shadowing, is frequently the main driver for electron losses between the LCDS and the plasmapause location. The minimum plasmapause position is often 1.0–1.5 Earth radii R_E lower than the minimum

LCDS. Consequently, ULF wave-driven radial diffusion is less likely to be the primary driver for losses at L-shells below the LCDS and above 1.5 R_E.

To calculate all these values, the International Radiation Belt Environment Modeling (IRBEM) library is utilized in conjunction with OMNI data, while employing the International Geomagnetic Reference Field IGRF-13 (Alken et al., 2021) and the Tsyganenko and Sitnov 2005 (TS05) models for the description of the internal and external geomagnetic field components.

With dropouts and REP events identified, it becomes feasible to ascertain whether dropouts coincide with precipitation events. For this study, the dropouts are separated into the two categories, based on the presence/ absence of MeV electron precipitation. The dropout events with precipitation are identified by fulfilling two criteria:

(1) Precipitation must be detected in an interval from 12 hours prior to the dropout commencement to 4 hours after its end. This temporal criterion aligns with the established definition of a dropout event, characterized by a rapid decline exceeding five units within an 8-hour interval (Xiang et al., 2018). Given the dataset's temporal resolution of 4 hours, the chosen window ensures full coverage of the 8-hour period before the dropout and at the time of the dropout end.

(2) The recorded precipitation must fall within a specified L-star range relative to the dropout location, set at ± 0.3, to accommodate potential inaccuracies in L-star calculations. While the maximum error in the calculations may exceed ± 0.3, the value is chosen as a conservative estimate. This decision is based on the observation that the overall number of detected dropouts with precipitation varies by only 4% between ± 0.3 and ± 0.6, but showed a 10% increase from ± 0.1 to ± 0.3 and a 4% increase from ± 0.6 to ± 0.7.

Events not satisfying these selection requirements are classified as dropouts without precipitation.

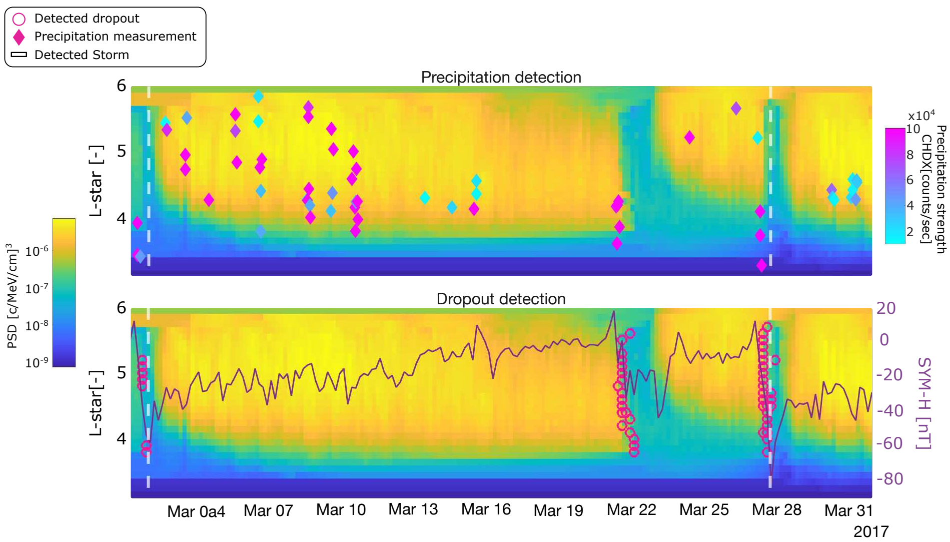

Figure 1: In the upper panel, the PSD is depicted overlaid with precipitation (diamonds) measured by CALET, with color indicating the strength of the precipitation in count rate. Detected storm events by Turner et al. (2019) are denoted by white dotted lines on both plots. The lower subfigure illustrates the PSD overlaid with dropout events (magenta circles) and the SYM-H index.

2.3 Potential sources of uncertainty

Utilizing the Van Allen Probes introduces the challenge of limited time resolution, which at best is approximately 4 hours. However, due to various factors such as data gaps, the time resolution can deteriorate, potentially resulting in the omission of dropout events. Furthermore, the nature of PSD necessitates fixed values for K and μ, making it challenging to capture all dropout events within the MeV energy band of CALET without conducting multiple iterations across different parameter values. Given that energy varies with L-star, this approach may result in potential undetected MeV dropouts during certain times and in specific L-star regions.

In addition to dropout detection, the precipitation measurements lead to potential uncertainties. As a result of the offset and tilt of the geomagnetic dipole with respect to the Earth, combined with the ISS orbital constraints, CALET is able to sample the outer radiation belt at varying L-shell/MLT intervals throughout its orbit (Bruno et al., 2021). Additionally, the coverage of the L-shell per MLT is not uniform. Moreover, the CALET measurements are reported in terms of L-shell values, representing drift-shell distance at magnetic equator, whereas for comparison purposes, L-star values are necessary, indicating regions characterized by stably trapped particles. The L-star calculation involves magnetic-field line tracing through the ISS position using the IGRF and the TS05 models. Subsequently, L-star is computed for the specified set of K values at the equatorial location. It's important to note that this methodology assumes that the particle precipitation is aligned with the magnetic field. The L-star values derived from both the Van Allen Probe dataset and the CALET dataset are accompanied by potential errors arising from the modeling of the Earth magnetic filed. Consequently, a threshold of ± 0.3 for L-star alignment is selected.

3 Analysis and Discussion

This study focuses on addressing two fundamental inquiries: the temporal occurrence and the spatial distribution of precipitation events in conjunction with dropout occurrences. If not specified otherwise, the adiabatic invariants $K = 1.311\text{G}^{1/2}$ and $\mu =$ 144MeV/G are employed to derive the forthcoming results. These values correspond to an energy range of 1.4 to 3.6 MeV and an equatorial pitch angle range of 12 to 25 degree, in an L-star range from 3-6. They were chosen due to their association with a relatively high occurrence of MeV dropouts and the possibility of waves being associated with this dropout, as this particle population can be efficiently scattered by He^{+}- and O^{+}-band EMIC waves (Xiang et al., 2018). As a result, this study encompasses a total of 106 events, with 63 instances occurring without precipitation and 43 being accompanied by precipitation. The dimensions of the dropouts are illustrated in Figure 2. The figure showcases the dimensions of all dropouts, encompassing both those with and without precipitation. The extension of L-star indicates the range over which the dropouts span. Notably, dropouts with precipitation tend to cover a broader L-star range compared to those without precipitation. To compute the factor of the PSD drop for a single dropout, the mean PSD reduction across each L-star bin where a decrease of at least a factor of five is observed. The values show that the dropout depth tends to be larger for dropouts with precipitation. While the maximum values of PSD drop for events with and without precipitation can be very large, such high values are rare occurrences rather than commonly observed features. The duration of dropouts, measured in hours, is determined by identifying the first and last detection across all L-star bins. Dropouts with precipitation tend to have longer durations.

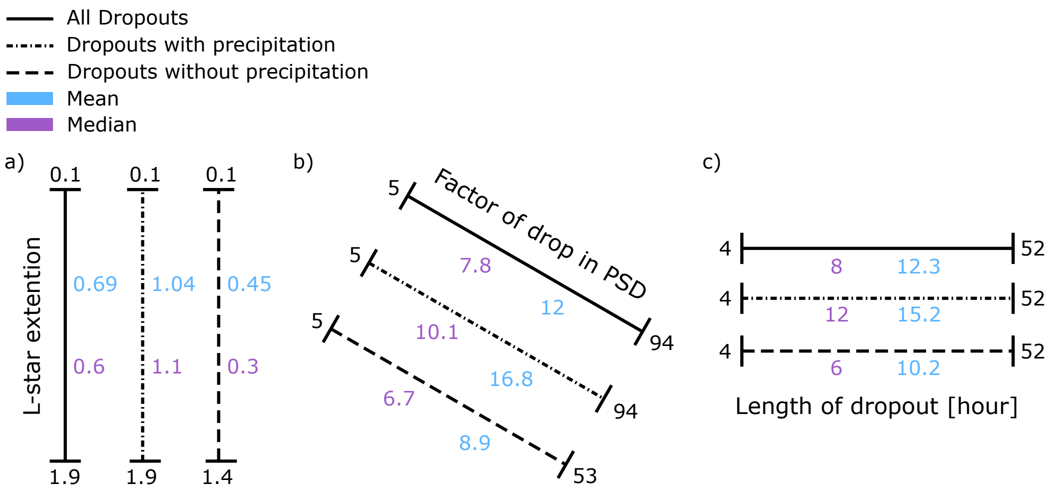

Figure 2: Dimension of dropouts, including the L-star extension, (a) drop in PSD, (b) and duration of dropout, (c) split into dropouts with and without precipitation. The dimensions are defined by the minimum and maximum values at the beginning and end of each line. The mean and median values are also reported in cyan and violet, respectively.

3.1 When - Temporal occurrence of dropout related precipitation

The temporal relationship between the onset of precipitation and dropout detection, as well as the timing of the SYM-H index drop, the peak in dynamic pressure P_{dyn}, and the direction of the interplanetary magnetic field (IMF) B_z component, is explored by evaluating a timeline. Thereby, a superposed epoch study is conducted using all identified dropout events with precipitation.

Figure 3(a) presents all precipitation measurements during the time of the detected dropouts and their strength in counts, while Figure 3(b) shows the probability distribution function (PDF) based on the amount of precipitation in (a) indicating the amount of precipitation during different times relative to the time of the dropout. Figure 3(c) shows the mean in the SYM-H index for all events, with dashed lines indicating the upper and lower quartiles. The same is done in Figure 3(d) for P_{dyn} and Figure 3(e) for B_z. The dropout start is delineated as the moment when the PSD experiences its initial decline exceeding a factor of five. Conversely, the end of the dropout is identified as the first instance where there is no further reduction of any magnitude in PSD observed. Preceding the dropout onset, time is measured absolutely, while the interval between dropout onset and conclusion is relative and contingent upon the duration of the dropout itself.

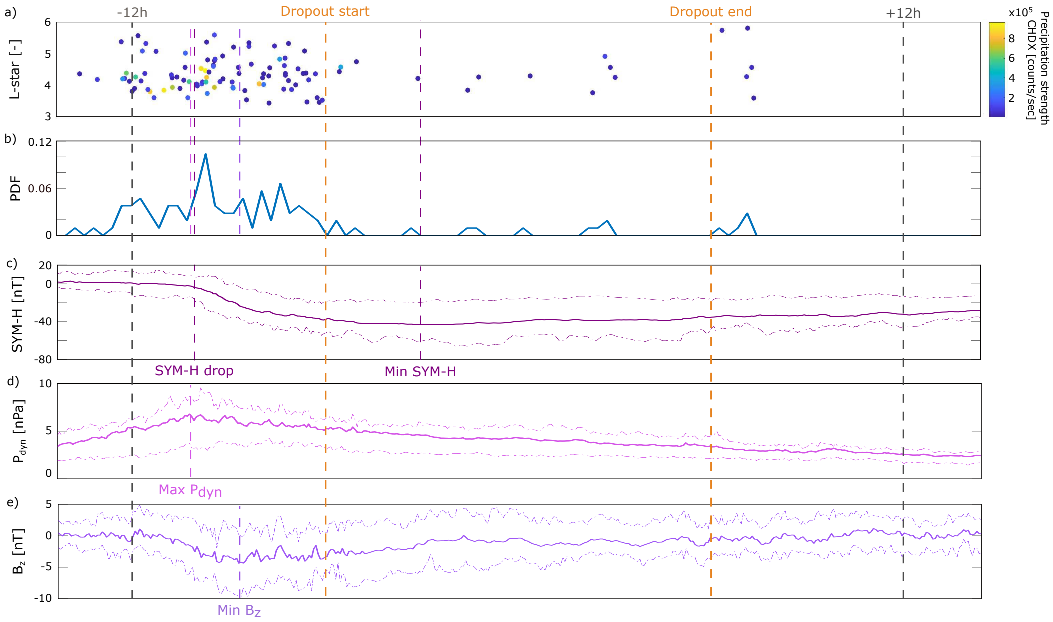

Figure 3: Timeline illustrating precipitation occurrence relative to dropout start and end times, overlaid with averaged maximum SYM-H index, maximum dynamic pressure P_{dyn}, and minimum magnetic field strength B_z of all events. Absolute time frames occur before and after dropout events, with relative time in between. a) Precipitation plotted in L-star over time, with color indicating precipitation strength measured in the CHDX channel of CALET in counts. b) Probability distribution of precipitation occurrence over time. c) Mean SYM-H index for all events with upper and lower quartiles (dashed line). d) Mean P_{dyn} for all events with upper and lower quartiles (dashed line). e) Mean B_z for all events with upper and lower quartiles (dashed line).

The drop in the SYM-H index occurs roughly 8.5 hours prior to the onset of dropouts, along with the peak in P_{dyn} and the drop in B_z. This is accompanied by heightened precipitation, indicating a correlation between the outlined values, and the commencement of precipitation associated with dropouts. A study by Ni et al. (2016) shows that for electrons with energies greater than 100 keV, the largest depletion occurs during or right after the peak in P_{dyn}. In this work, the peak in MeV precipitation can be observed roughly 7.5 hours before the dropout is detected, following the peak in P_{dyn}. While earlier studies proposed that precipitation of high-energy electrons into the Earth's atmosphere occur mainly during the recovery phase of the SYM-H index (Bazilevskaya et al., 2017; Horne et al., 2009), the used dataset indicates a larger amount of precipitation before the dropout onset. A study conducted by Mourenas et al. (2016) demonstrated how the combination of chorus and EMIC waves could induce rapid MeV dropouts, within the observed timeframe (2-10 hours), at an L-range of 3-6. After the onset of dropouts, there is a rapid decrease in precipitation amount, attributed to the significant loss of electrons that has already occurred by the time dropouts are detected. During the time of the dropout, the minimum in the SYM-H index is reached. As the dropout progresses, precipitation diminishes gradually, with precipitation levels nearly absent by the end of the dropout phase. Regarding the precipitation strength, defined by the amplitude in count rate measurements of CALET, it is highest during the phase of the drop in the minimum SYM-H index and decreases over time.

Analysis of the dataset from 2015 to 2019 reveals a trend associated with the solar cycle and the seasons, indicating changes in dropout frequency, as well as variations in the frequency of dropouts with associated precipitation. Figure 4a presents the study by Mursula et al. (2022), illustrating the annual distribution of storms driven by CMEs and HSSs/CIRs. This categorization is used to better contextualize the data in Figure 4b, which illustrates the trend of sunspot numbers over time, with overlaid bars indicating dropout occurrences separated into those without precipitation and those accompanied by precipitation. The data show that with a required alignment between dropouts and precipitation events of $L^{*}\pm0.3$, the decrease in occurrence towards the solar minimum is only evident from 2017 to 2018, with fewer dropout events observed in 2016 compared to 2017. However, it's necessary to note that certain time periods are subject to small-number statistics. As outlined in Section 2.3, due to specific K and μ values and the energy dependence of electrons relative to L^{*}, some dropouts in different L^{*} regions might not be detected. Conversely, loosening the criteria risks categorizing dropouts as those with precipitation, even if the precipitation occurred independently. Nonetheless, to assess overall trends and gauge sensitivity, an L^{*} alignment requirement of ±1 is additionally set, as shown by the shaded bars in Figure 4b. The results in Figure 4b show similar trends for both alignment criteria overall, with larger discrepancies observed in 2016. However, the primary focus in the following analysis is on the stricter binning criteria of ±0.3 to eliminate the number of potential false positive dropout categorizations.

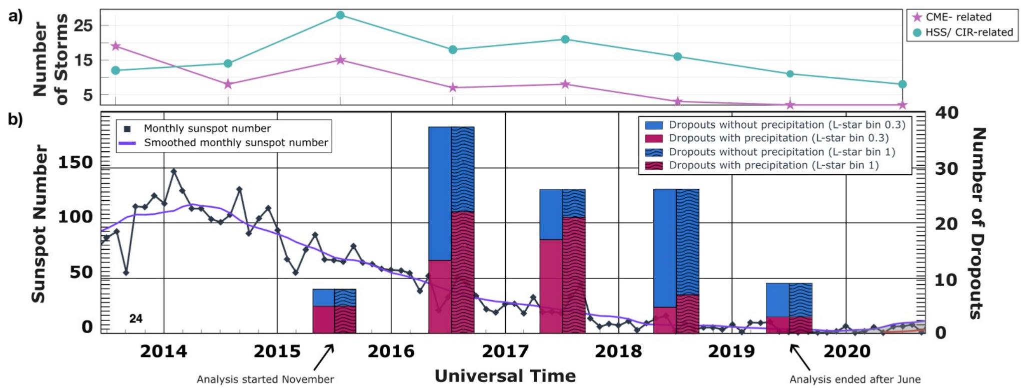

Figure 4: A comparative analysis of yearly dependency of detected dropouts. a) Number of different storm types per year as comparison (Mursula et al., 2022) b) Number of detected dropouts($K = 1.311\,\mathrm{G}^{1/2}\mathrm{R}_E$, $\mu = 144\,\mathrm{MeV/G}$) with and without precipitation alignment (Magenta vs. Blue) within an L-star alignment requirement of ±0.3 and ±1 including data from the beginning of November 2015 until the end of June 2019, plotted against the solar cycle sunspot numbers (NOAA, 2024).

The seasonal variation, along with the potential correlation between dropouts with and without precipitation and the equinoxes, is depicted in Figure 5. Thereby, only the years with full measurement coverage (2016-2018) are included. Figure 5(a) illustrates fluctuations in the total number of dropouts, while Figure 5(b) depicts variations in the percentage of dropouts accompanied by precipitation per month. Both Figure 5(a) and 5(b) reveal peaks around the spring and autumn equinoxes, marked by the Sun's crossing of the celestial equator.

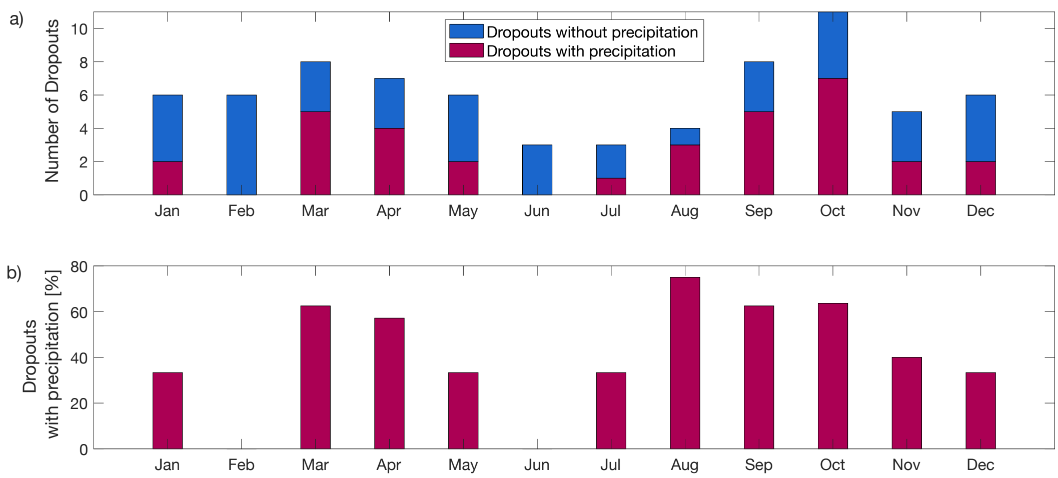

Figure 5: A comparative analysis of monthly dependency of detected dropouts ($K = 1.311\,\mathrm{G}^{1/2}\mathrm{R}_E$, $\mu = 144\,\mathrm{MeV/G}$) within a variability in L-Star of ±0.3. a) Comparison between dropouts with and without precipitation alignment (Magenta vs. Blue) per month. b) Percentage of dropouts with precipitation per month.

The observed trend with the solar cycle in Figure 4 is likely attributable to the decline in solar activity leading towards the solar minimum, resulting in fewer geomagnetic disturbances (Miyoshi & Kataoka, 2011; Samsonov et al., 2019; Mursula et al., 2022). The annual as well as the semiannual variation is also reported by Vidal-Luengo et al. (2024) for all MeV precipitation events measured by CALET. However, from 2017 to 2018, the number of dropouts with precipitation decreases drastically, while the total number of dropouts remains the same.

The decrease in events with precipitation may be attributed to variations in electron intensity stemming from changes in geomagnetic activity. Typically 2-3 years before reaching the solar minimum there is an uptick in high-speed solar wind streams (HSSs) and a decrease in interplanetary coronal mass ejections (CMEs) (Richardson et al., 2001), as can be seen in Figure 4a. These streams energize the radiation belt whenever the solar wind velocity exceeds 500 km/s (Baker & Kanekal, 2008). The importance of HSS events for the energetic particle population in the outer radiation belt, coupled with the lower occurrence rate in 2016 compared to 2017, could potentially explain why no decrease of precipitation-related dropouts can be seen in the data from 2016 compared to 2017, even while approaching solar minimum.

Additionally, HSS-events lead to pronounced seasonal variations, depicted in Figure 5 and observed during this descending phase from approximately 2015-2018 by Katsavrias et al. (2021). The seasonal variation in average flux reveals peaks during spring (February to April) and fall (August to October) for electrons within the 2-6 MeV range at $2.5 < L < 6.5$. In contrast, electron flux decreases notably during winter (November to January) and further diminishes in summer (May-June) (Baker & Kanekal, 2008). This variation is primarily driven by the Russell–McPherron effect (Russell & McPherron, 1973), which stems from the larger z component of the interplanetary magnetic field near the equinoxes in GSM coordinates, resulting from the tilt of the dipole axis relative to the heliographic equatorial plane. Additionally, the equinoctial effect (Cliver et al., 2000, 2002), representing the varying angle of the Earth's dipole with respect to the Earth–Sun line and consequently the solar wind speed, particularly when the angle is at 90° during the equinoxes, cannot be excluded as a contributing factor (Katsavrias et al., 2021).

The findings of Mursula et al. (2022) corroborate the theory that HSS events are important for dropout events with precipitation by revealing a significant decrease in moderate HSS events between 2017 and 2018. However, the overall storm frequency, including CMEs and weak HSS-events, remains relatively stable during this period. The prevalence of MeV dropouts may remain high due to the influence of weaker storms, which, at the same time, might not be strong enough to induce precipitation. In support of this, 2018 exhibits smaller average dropout dimensions, accompanied by lower average minimum SYM-H indices. Solar wind parameters and geomagnetic indices may also exert additional influence.

The enhanced geomagnetic activity during the equinoxes manifests, among other things, in a distinct seasonal variation of the DST index (Oh & Yi, 2011). Therefore, the potential link between precipitation events and increased geomagnetic activity is explored next by examining their association with storms using the minimum SYM-H index. Thereby, the DST index and the SYM-H only differentiate in the time resolution of 1 hour and 1 minute, respectively. The minimum SYM-H for each event is determined by identifying the lowest value within the time period of 12 hours preceding the dropout until the end of the dropout. A minimum SYM-H categorization commonly used to classify storm intensity is as follows (Loewe & Prölss, 1997): a weak storm is defined as $-30\,\text{nT} > \text{SYM-H} > -50\,\text{nT}$, a moderate storm as $-50\,\text{nT} > \text{SYM-H} > -100\,\text{nT}$, and a strong storm as $-100\,\text{nT} > \text{SYM-H} > -200\,\text{nT}$. Figure 6 illustrates the SYM-H dependency of dropouts with and without precipitation. Applying this definition of storms, it becomes apparent that dropouts do not always occur in relation to a storm. Furthermore, even dropouts with precipitation sometimes transpire for SYM-H minimum indices below the threshold defined for a weak storm of $-30\,\mathrm{nT}$.

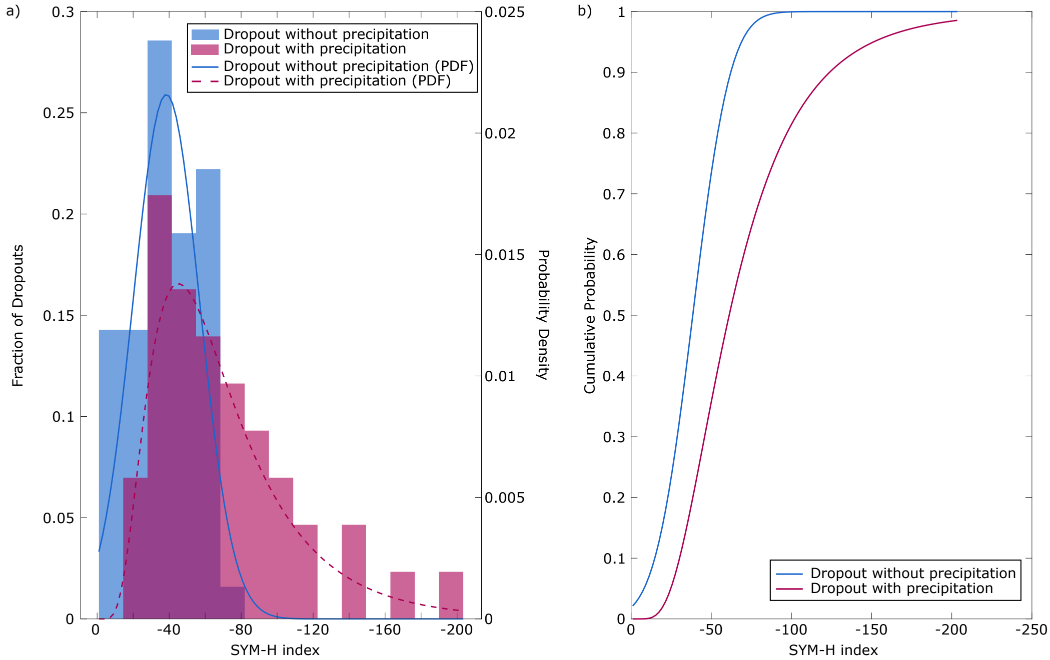

Figure 6: SYM-H index dependency of detected dropouts ($K = 1.311\,\mathrm{G}^{1/2}\mathrm{R}_E$, $\mu = 144\,\mathrm{MeV/G}$) with and without precipitation alignment (Magenta vs. Blue) within a variability in L-Star of ± 0.3. a) Fraction of dropouts with precipitation indicates to follow a log normal distribution, while dropouts without precipitation alignment indicate to follow a normal distribution. b) Cumulative probability indicating the occurrence of all dropouts without precipitation during more positive SYM-H indices and vice versa.

Figure 6(a) shows that dropouts associated with precipitation exhibit a normal distribution, while those without precipitation follow a lognormal distribution, as confirmed by the Kolmogorov-Smirnov Test. Moreover, Figure 6(b) demonstrates that dropouts consistently coincide with precipitation for SYM-H minimum indices more negative than -85. Conversely, when the SYM-H minimum index is more positive than -15, precipitation in correlation with dropout events is not observed. The findings suggest that a magnetosphere undergoing heightened disturbance is more predisposed to initiating precipitation events, potentially due to an amplification in wave occurrence. An earlier study by Ni et al. (2016) showed additionally that electron flux dropouts become more significant when the magnitude of SYM-H index decreases largely. Meredith et al. (2011) proposed that belt dropouts during the main phase of HSS driven storms are not caused by precipitation to the atmosphere. However, this study indicates that any storms can be at least accompanied by MeV electron precipitation if the disturbance of the magnetosphere is strong enough.

When examining the temporal profiles of P_{dyn} and B_z, the differentiation between dropouts with and without precipitation becomes less distinct, as shown in Figure 7. Similar to the determination of the minimum SYM-H, the peak in P_{dyn} and the minimum in B_z for each event are identified by finding the lowest value within the time period spanning 12 hours before the onset of dropout until its end. Dropouts with precipitation tend to occur in relation to more positive P_{dyn} values and more negative B_z values. The former is likely due to magnetosphere compression and the resulting waves (Onsager et al., 2002; Yan et al., 2023). A study by Yu et al. (2013) supports the observed trend, as similar results indicate that higher values of $P_{\rm dyn}$ correspond to more significant MeV electron flux dropouts compared to lower values of $P_{\rm dyn}$. The latter is likely due to the fact that a southward IMF B_z results in strong injections from the plasma sheet, providing a source of free energy for electromagnetic wave excitation, which in turn leads to wave-particle interaction (Gao et al., 2015).

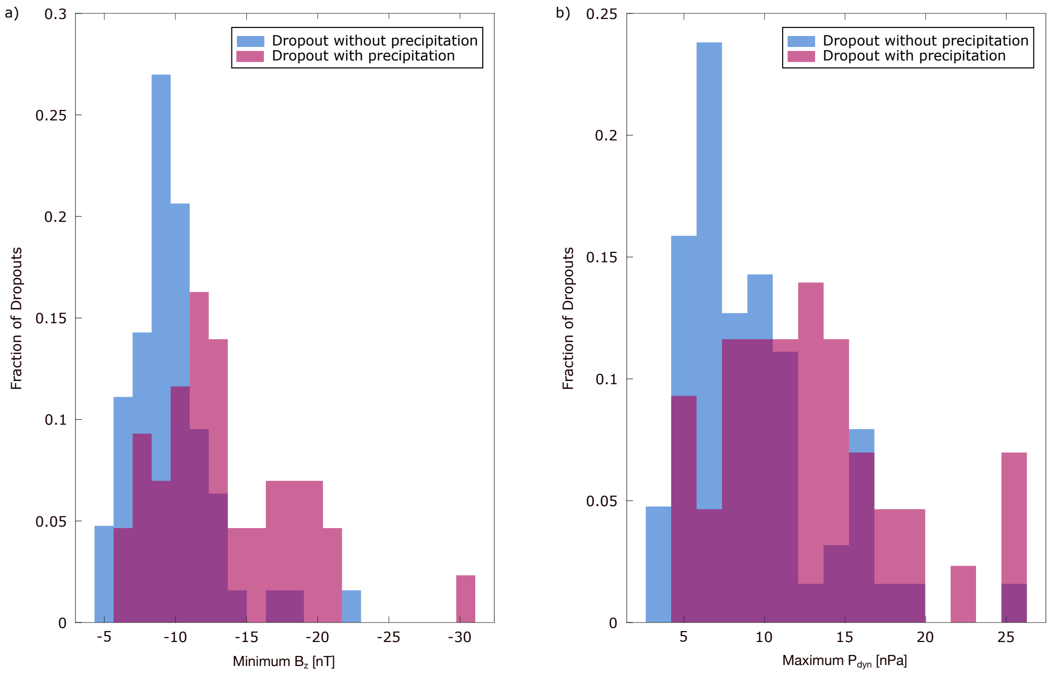

Figure 7: B_z and P_{dyn} dependency of detected dropouts ($K = 1.311\,\mathrm{G}^{1/2}\mathrm{R}_E$, $\mu = 144\,\mathrm{MeV/G}$) with and without precipitation alignment (Magenta vs. Blue) within a variability in L-Star of ± 0.3. a) Fraction of dropouts for a given B_z minimum. b) Fraction of dropouts for a given P_{dyn} maximum.

Investigating the relationship between dropout events with and without precipitation and the LCDS helps to identify the dropout mechanism, whether solely due to precipitation or a combination of factors like precipitation, magnetopause shadowing, and outward radial diffusion. Figure 8 illustrates a direct correlation between the SYM-H index and the LCDS. Specifically, Figure 8(a) displays the fraction of dropouts with and without precipitation alongside the corresponding LCDS. It can be seen that for an LCDS value smaller than 6.5, all detected dropouts were accompanied by precipitation. This indicates that the likelihood of a dropout being associated with precipitation increases as the LCDS moves inward, and decreases as the LCDS moves outward. Figure 8(b) illustrates the relationship between the SYM-H index and the LCDS, showing a direct correlation between these values. This observation is noteworthy, because events where the LCDS moves far inward are often attributed solely to magnetopause shadowing and outward radial diffusion. However, the research indicates that all three mechanisms contribute to dropouts associated with low LCDS values and consequently more negative SYM-H indices.

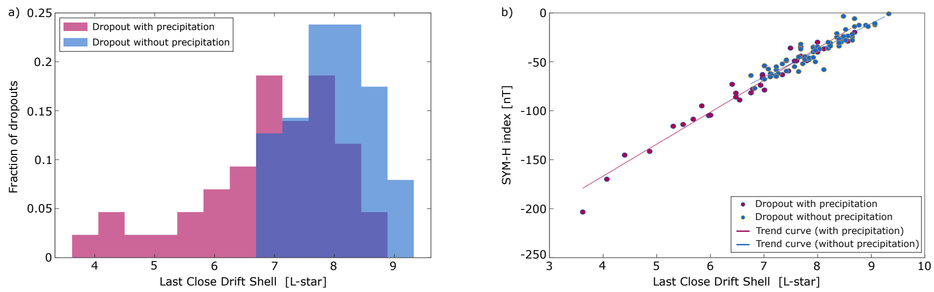

Figure 8: Detected Dropouts ($K = 1.311\,\mathrm{G}^{1/2}\mathrm{R}_E$, $\mu = 144\,\mathrm{MeV/G}$) with and without Precipitation Alignment (Magenta vs. Blue) within a Variability in L-Star of ±0.3, presented as: a) Fraction of dropouts per Last Close Drift Shell. b) Dropout distribution per SYM-H index per Last Close Drift Shell.

3.2 Where - Spatial occurrence of dropout related precipitation

To examine disparities in spatial occurrence between dropouts with and without precipitation, the study investigates the penetration depth, denoting the minimum L-star value at which the dropout is detected. Figure 9 illustrates the penetration depth of dropouts with precipitation (magenta) and without precipitation (blue). The graph highlights a noticeable distinction between dropouts with and without precipitation. Dropouts associated with precipitation tend to penetrate into deeper L-star regions, with the highest occurance below an L-star value of 4, while dropouts without precipitation tend to penetrate less deeply, leading to a peak occurrence above an L-star value of 5. This result suggests two possibilities: firstly, that precipitation plays a pivotal role in dropouts occurring within low L-star regions, or secondly, that dropouts associated with loss within these regions coincide with precipitation events. Figure 9 also reveals outliers of dropouts with precipitation events in higher L-star regions, and vice versa.

While studies have shown that magnetopause shadowing tends to be the predominant loss mechanism at L-star > 4, and EMIC waves can significantly contribute to electron loss at L-star < 4 (Shprits et al., 2006; Turner, Shprits, et al., 2012; Xiang et al., 2018), the reverse can also be true (Xiang et al., 2017).

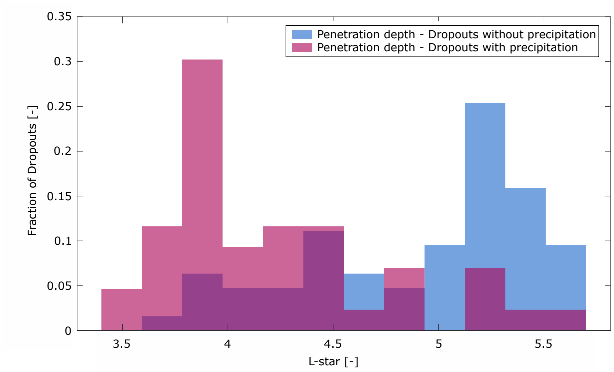

Figure 9: Penetration depth dependency in L-star of detected dropouts ($K = 1.311\,\mathrm{G}^{1/2}\mathrm{R}_E$, $\mu = 144\,\mathrm{MeV/G}$) with and without precipitation alignment (Magenta vs. Blue) within a variability in L-Star of ±0.3, indicated by plotting the fraction of the dropouts over L-star.

Besides the L-star region, the pronounced MLT region of precipitation occurrence is investigated. Figure 10(a) illustrates the fraction of occurrences of precipitation not associated with a dropout in purple, while the pink color indicates precipitation correlated with dropouts. Overall, these two datasets align with each other, albeit with a more pronounced trend observed for precipitation with dropouts occurring in the dusk and midnight sector.

Precipitation in the dusk sector has frequently been observed in correlation with a strong southward IMF B_z, consistent with the trend depicted in Figure 7(a) (Gao et al., 2015). EMIC waves are proposed as the primary driver of loss (Horne et al., 2009; Gao et al., 2015). During the compression of the magnetic field induced by P_{dyn}, it was suggested that EMIC waves become excited and manifest around MLT 18 (Yan et al., 2023). While the trend of higher dynamic pressure leading to dropout events is evident in Figure 7(b), the dependence is not distinct. Precipitation in the midnight sector has been previously observed during periods characterized by either strong southward IMF B_z or high dynamic pressure (Gao et al., 2015). It is suggested that precipitation around the midnight sector may be primarily driven by CSS. Hiss and Chorus waves alone are unlikely to serve as the primary driver in the dusk and midnight sectors due to their distribution of occurrence (Borovsky, 2021). Although the occurrence rate of MeV dropouts does not exhibit a clear dependence on MLT (Hua et al., 2023; Onsager et al., 2002), a discernible precipitation trend is evident. This suggests that precipitation may primarily influence MeV dropouts around the dusk-midnight sector.

Figure 10(b) shows all precipitation measurements related to a dropout event, with color indicating the precipitation strength in counts per second plotted along L-star. Most of the precipitation occurs between L-star of 4 and 5, with the strongest precipitation events occuring during the periods of dusk and midnight, especially around MLT 19-20, as also noted by Jordanova et al. (2008).

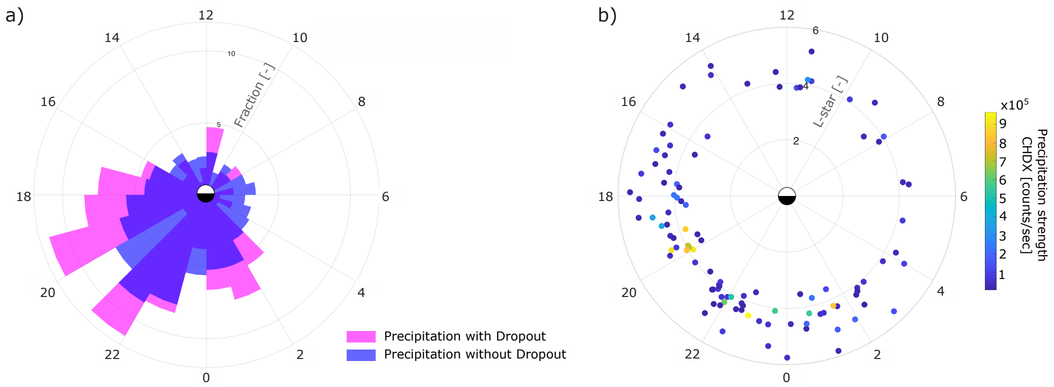

Figure 10: a) Analysis of the MLT dependency of precipitation with and without dropout alignment ($K = 1.311\,\mathrm{G}^{1/2}\mathrm{R}_E$, $\mu = 144\,\mathrm{MeV/G}$), represented by Pink and Purple respectively, within a Variability in L-Star of ± 0.3. The data is binned into 1-hour MLT regions and displayed as fractions. b) Visualization of precipitation measurements with dropout alignment plotted against MLT and L-star, with color indicating precipitation strength measured by the CHDX channel of CALET.

3.3 Validation

All the trends observed in the analysis outlined in Chapter 3.1 and 3.2 are replicated using a different set of K and μ values, with K being 0.172 $G^{1/2}R_E$ and μ being 1096 MeV/G, corresponding to a similar energy range of 1.4 to 4.2 MeV and a equatorial pitch angle range of 35 to 58 degrees. In total, 91 dropouts are found, with 35 of them associated with precipitation. The same trend for B_z and P_{dyn} depicted in Figure 7 is even more pronounced at these K and μ values.

Furthermore, it is tested whether precipitation consistently occurs at the same rate or if there is an enhancement around the time of the dropout occurrence. This validation aims to ensure that the timeline depicted in Figure 3 is not merely a random alignment of precipitation points. A 10-day time frame is chosen both before and after the onset of dropouts, during which the precipitation is documented, as illustrated in Figure 11(a). Figure 11(b) displays the PDF over time, indicating the precipitation amount. It is evident that a significant increase in precipitation events occurs between 11h and 9h before the detection of dropout commencement. This validates that the chosen time period of Figure 3, which is 12 hours, aligns well with the precipitation occurrence observed over a longer duration and is not random. Furthermore, a slight decrease in L-star just before the commencement of dropout can be observed in Figure 11(a).

To further validate the temporal relationship between dropouts and precipitation events, a low-energy population is selected. This population, characterized by specific values of $K = 0.015$ $G^{1/2}R_E$ and $\mu = 50$ MeV/G, corresponds to an energy range around 117 keV and an equatorial pitch angle around 77 degrees. Precipitation measurements using CALET's energy channels are not feasible within this range, implying that there should be no correlation between dropouts and precipitation events. All dropout events previously identified within the MeV range have been omitted from consideration due to the potential for precipitation originating from those dropouts. Following the implementation of binning in L-star at ± 0.3 and subsequent reevaluation, only approximately 4% of events are found to correlate with precipitation, indicating the success of the test.

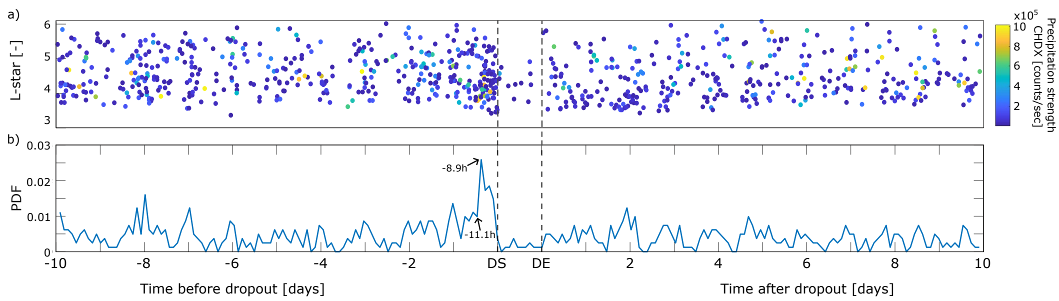

Figure 11: Timeline illustrating precipitation occurrence relative to dropout start (DS) and end (DE) times, overlaid with averaged maximum SYM-H, maximum dynamic pressure P_{dyn}, and minimum magnetic field strength B_z of all events. Absolute time frames occur before and after dropout events, with relative time in between. a) Precipitation plotted in L-star over time, with color indicating precipitation strength measured in the CHDX channel of CALET in counts. b) Probability distribution of precipitation occurrence over time.

4 Summary and Conclusions

The study yields several key conclusions concerning the temporal and spatial occurrence of MeV electron precipitation in relation to radiation belt dropouts:

- Dropouts with MeV precipitation typically exhibit larger dimensions (L-star extension, factor of drop in PSD, and length) compared to those without precipitation.
- Precipitation tends to occur during periods of SYM-H and B_z decline, as well as enhancements in P_{dyn}. These conditions also lead to the largest amplitude of precipitation, predominantly in lower L-star regions.
- The total number of dropouts, as well as fraction of dropouts with precipitation, show a correlation with the solar cycle and the seasons, likely attributable to solar and geomagnetic activity.
- During periods of more negative minimum SYM-H indices, which coincide with the inward movement of LCDS, the likelihood of experiencing dropouts with precipitation significantly increases.
- A tendency is observed where lower B_z and larger P_{dyn} values are more likely to be associated with precipitation during dropouts.
- Dropouts accompanied by precipitation tend to penetrate into lower L-star regions.
- The occurrence of precipitation associated with dropout events peaks in the dusk-midnight sector, coinciding with an increase in precipitation intensity.

Overall, this study provides initial insights into the contribution of precipitation into the atmosphere to radiation belt losses observed during MeV dropout events. Evidence is provided showing that precipitation frequently occurs during MeV dropouts, emphasizing its importance as a loss mechanism. These findings support that precipitation is needed as an additional mechanism in simulations to capture the full extent of electron loss during MeV dropouts. Additionally, these results demonstrate a distinction between MeV electron dropouts with and without precipitation, highlighting their dependence on solar wind parameters, geomagnetic indices, dropout dimensions, and MLT.

Data Availability Statement

The CALET data utilized in this research are publicly accessible online in ASCII format through the Data ARchives and Transmission System of the Japan Aerospace Exploration Agency (`data.darts.isas.jaxa.jp/pub/calet/cal-v1.1/CHD/level1.1/obs/`). Additionally, the combined pitch-angle resolved electron flux data from Van Allen Probes A and B are available via `https://rbsp-ect.newmexicoconsortium.org/rbsp_ect.php`, along with the corresponding Magnetic Ephemeris data (`https://rbsp-ect.newmexicoconsortium.org/science/DataDirectories.php`). Furthermore, NASA's OMNIWeb data can be accessed online at `https://cdaweb.gsfc.nasa.gov`.

Acknowledgments

D. Freund, L. W. Blum, A. Bruno and S.Vidal-Luengo acknowledge support from NASA/Living With a Star Science program NNH20ZDA001N-LWS, and the NSF AGS-2123253 grant. A. Bruno also acknowledges support by NASA under award number 80GSFC21M0002. R. Kataoka acknowledges support from JSPS Kakenhi grant 24H00025. Appreciation is extended to the CALET collaboration and the Van Allen Probes team for providing the data.

References

Alken, P., Thébault, E., Beggan, C., et al. (2021). International geomagnetic reference field: the thirteenth generation. *Earth, Planets and Space*, *73*(49). Retrieved from `https://doi.org/10.1186/s40623-020-01288-x` doi: 10.1186/s40623-020-01288-x

Allen, R. C., Zhang, J.-C., Kistler, L. M., Spence, H. E., Lin, R.-L., Klecker, B., … Jordanova, V. K. (2015). A statistical study of emic waves observed by cluster: 1. wave properties. *J. Geophys. Res. Space Physics*, *120*, 5574–5592. doi: 10.1002/2015JA021333

Baker, D. N., Blake, J. B., Callis, L. B., Cumming, J. R., Hovestadt, S., D .and Kanekal, Klecker, B., … Zwick, R. D. (1994, Mar). Relativistic electron acceleration and decay timescales in the inner and outer radiation belts: Sampex. *Geophysical Research Letters*, *21*(6), 409–412.

Baker, D. N., Kanekal, S., Hoxie, V., Batiste, S., Bolton, M., Li, X., … Friedel, R. (2013). The relativistic electron-proton telescope (rept) instrument on board the radiation belt storm probes (rbsp) spacecraft: Characterization of earth's radiation belt high-energy particle populations. *Space Sci Rev*, *179*, 337–381. (Received: 12 April 2012 / Accepted: 9 October 2012 / Published online: 14 December 2012 © Springer Science+Business Media Dordrecht 2012) doi: 10.1007/s11214-012-9950-9

Baker, D. N., & Kanekal, S. G. (2008). Solar cycle changes, geomagnetic variations, and energetic particle properties in the inner magnetosphere. *Journal of Atmospheric and Solar-Terrestrial Physics*, *70*(2–4), 195–206. Retrieved from `https://doi.org/10.1016/j.jastp.2007.08.031` doi: 10.1016/j.jastp.2007.08.031

Bazilevskaya, G. A., Kalinin, M. S., Krainev, M. B., Makhmutov, V. S., Svirzhevskaya, A. K., Svirzhevsky, N. S., … Gvozdevsky, B. B. (2017). Precipitation of magnetospheric electrons into the earth's atmosphere and the electrons of the outer radiation belt. *Bulletin of the Russian Academy of Sciences: Physics*, *81*(2), 215–218. (Original Russian Text published in Izvestiya Rossiiskoi Akademii Nauk, Seriya Fizicheskaya) doi: 10.3103/S1062873817020071

Blake, J., Carranza, P., Claudepierre, S., Clemmons, J., Crain Jr., W., Dotan, Y., … Zakrzewski, M. (2013). The magnetic electron ion spectrometer (mageis) instruments aboard the radiation belt storm probes (rbsp) spacecraft. *Space Sci Rev*, *179*, 383–421. (Received: 15 October 2012 / Accepted: 9 May 2013 / Published online: 7 June 2013 © The Author(s) 2013. This article is published with open access at Springerlink.com) doi: 10.1007/s11214-013-9991-8

Blum, L. W., Bruno, A., Capannolo, L., Ma, Q., Kataoka, R., Torii, S., & Baishev, D. (2024). On the spatial and temporal evolution of emic wave-driven relativistic electron precipitation: Magnetically conjugate observations from the van allen probes and calet. *Geophysical Research Letters*, *51*, e2023GL107087. (Received 30 OCT 2023, Accepted 10 FEB 2024) doi: 10.1029/2023GL107087

Borovsky, J. E. (2021). Magnetospheric plasma systems science and solar wind plasma systems science: The plasma-wave interactions of multiple particle populations. *Frontiers in Astronomy and Space Sciences*, *8*, 780321. doi: 10.3389/fspas.2021.780321

Boyd, A. J., Spence, H. E., Reeves, G. D., Funsten, H. O., Skoug, R. M., Larsen, B. A., … Jaynes, A. N. (2021, February 11). Rbsp-ect combined pitch angle resolved electron flux data product. *Journal of Geophysical Research: Space Physics*, *126*(3), e2020JA028637. Retrieved from `https://doi.org/10.1029/2020JA028637` (Technical Reports: Data, Free Access) doi: 10.1029/2020JA028637

Bruno, A., Blum, L. W., de Nolfo, G. A., Kataoka, R., Torii, S., Greeley, A. D., et al. (2022). Emic-wave driven electron precipitation observed by calet on the international space station. *Geophysical Research Letters*, *49*, e2021GL097529.

(Received 3 JAN 2022, Accepted 23 FEB 2022) doi: 10.1029/2021GL097529

Bruno, A., Guzik, T. G., Nolfo, G. D., Blum, L., Cannady, N., & Ficklin, A. W. (2021, January). Relativistic electron precipitation observations with calet. In *43rd cospar scientific assembly* (Vol. 43, p. 1165).

Büchner, J., & Zelenyi, L. M. (1989, September). Regular and chaotic charged particle motion in magnetotaillike field reversals: 1. basic theory of trapped motion. *Journal of Geophysical Research*, *94*(A9), 11821–11842.

Capannolo, L., Li, W., Millan, R., Smith, D., Sivadas, N., Sample, J., & Shekhar, S. (2022). Relativistic electron precipitation near midnight: Drivers, distribution, and properties. *Journal of Geophysical Research: Space Physics*, *127*, e2021JA030111. doi: 10.1029/2021JA030111

Cliver, E. W., Kamide, Y., & Ling, A. (2002). The semiannual variation of geomagnetic activity: phases and profiles for 130 years of aa data. *Journal of Atmospheric and Solar-Terrestrial Physics*, *64*, 47–53. Retrieved from https://doi.org/10.1016/S1364-6826(01)00093-1 doi: 10.1016/S1364-6826(01)00093-1

Cliver, E. W., Kamide, Y., & Ling, A. G. (2000). Mountains vs. valleys: the semiannual variation of geomagnetic activity. *Journal of Geophysical Research*, *105*, 2413–2424. Retrieved from https://doi.org/10.1029/1999JA900439 doi: 10.1029/1999JA900439

Dachev, T. P. (2018). Relativistic electron precipitation bands in the outside radiation environment of the international space station. *Journal of Atmospheric and Solar-Terrestrial Physics*, *177*, 247–256. doi: 10.1016/j.jastp.2017.11.008

Drozdov, A. Y., Usanova, M. E., Hudson, M. K., Allison, H. J., & Shprits, Y. Y. (2020). The role of hiss, chorus, and emic waves in the modeling of the dynamics of the multi-mev radiation belt electrons. *Journal of Geophysical Research: Space Physics*, *125*, e2020JA028282. doi: 10.1029/2020JA028282

Friedel, R., Reeves, G., & Obara, T. (2002). Relativistic electron dynamics in the inner magnetosphere— a review. *Journal of Atmospheric and Solar-Terrestrial Physics*, *64*, 265–282.

Gao, X., Li, W., Bortnik, J., Thorne, R. M., Lu, Q., Ma, Q., ... Wang, S. (2015). The effect of different solar wind parameters upon significant relativistic electron flux dropouts in the magnetosphere. *Journal of Geophysical Research: Space Physics*, *120*, 4324–4337. doi: 10.1002/2015JA021182

Gokani, S. A., Kosch, M., Clilverd, M., Rodger, C. J., & Sinha, A. K. (2019). What fraction of the outer radiation belt relativistic electron flux at l ≈ 3–4.5 was lost to the atmosphere during the dropout event of the st. patrick's day storm of 2015? *Journal of Geophysical Research: Space Physics*, *124*, 9537–9551. doi: 10.1029/2018JA026278

Goldberg, R. A., Baker, D. N., Herrero, F. A., Jackman, C. H., Kanekal, S., & Twigg, P. A. (1995). Mesospheric heating during highly relativistic electron precipitation events. *Journal of Geomagnetism and Geoelectricity*, *47*, 1237–1247. (Received November 28, 1994; Revised June 12, 1995; Accepted June 23, 1995)

Green, J. C., & Kivelson, M. G. (2004). Relativistic electrons in the outer radiation belt: Differentiating between acceleration mechanisms. *Journal of Geophysical Research*, *109*, A03213. (Received 21 July 2003; revised 21 November 2003; accepted 22 January 2004; published 18 March 2004) doi: 10.1029/2003JA010153

Horne, R. B., Lam, M. M., & Green, J. C. (2009). Energetic electron precipitation from the outer radiation belt during geomagnetic storms. *Geophysical Research Letters*, *36*(L19), L19104. doi: 10.1029/2009GL040236

Hua, M., Bortnik, J., & Ma, D. (2023). Dependence of electron flux dropouts in the earth's outer radiation belt on energy and driving parameters during geomagnetic storms. *Journal of Geophysical Research: Space Physics*, *128*, e2023JA031882. Retrieved from https://doi.org/10.1029/2023JA031882 doi: 10.1029/2023JA031882

Jordanova, V. K., Albert, J., & Miyoshi, Y. (2008). Relativistic electron precipitation by emic waves from self-consistent global simulations. *Journal of Geophysical Research*, *113*, A00A10. doi: 10.1029/2008JA013239

Kataoka, R., Asaoka, Y., Torii, S., Nakahira, S., Ueno, H., Miyake, S., et al. (2020). Plasma waves causing relativistic electron precipitation events at international space station: Lessons from conjunction observations with arase satellite. *Journal of Geophysical Research: Space Physics*, *125*, e2020JA027875. (Received 2 FEB 2020, Accepted 3 AUG 2020, Accepted article online 14 AUG 2020) doi: 10.1029/2020JA027875

Kataoka, R., Asaoka, Y., Torii, S., Terasawa, T., Ozawa, S., Tamura, T., … Mori, M. (2016). Relativistic electron precipitation at international space station: Space weather monitoring by calorimetric electron telescope. *Geophysical Research Letters*, *43*, 4119–4125. (Received 4 APR 2016, Accepted 22 APR 2016, Accepted article online 25 APR 2016, Published online 7 MAY 2016) doi: 10.1002/2016GL068930

Katsavrias, C., Papadimitriou, C., Aminalragia-Giamini, S., Daglis, I. A., Sandberg, I., & Jiggens, P. (2021). On the semi-annual variation of relativistic electrons in the outer radiation belt. *Annales Geophysicae*, *39*, 413–425. Retrieved from https://doi.org/10.5194/angeo-39-413-2021 doi: 10.5194/angeo-39-413-2021

Loewe, C. A., & Prölss, G. W. (1997). Classification and mean behavior of magnetic storms. *Journal of Geophysical Research: Space Physics*, *102*(A7), 14029–14740. Retrieved from https://doi.org/10.1029/96JA04020 doi: 10.1029/96JA04020

Loto'aniu, T. M., Singer, H. J., Waters, C. L., Angelopoulos, V., Mann, I. R., Elkington, S. R., & Bonnell, J. W. (2010). Relativistic electron loss due to ultralow frequency waves and enhanced outward radial diffusion. *Journal of Geophysical Research*, *115*, A12245. doi: 10.1029/2010JA015755

Mauk, B. H., Fox, N. J., Kanekal, S. G., et al. (2013, November). Science objectives and rationale for the radiation belt storm probes mission. *Space Science Reviews*, *179*, 3–27. Retrieved from https://doi.org/10.1007/s11214-012-9908-y (Received: 01 February 2012; Accepted: 02 June 2012; Published: 07 September 2012) doi: 10.1007/s11214-012-9908-y

Meredith, N. P., Horne, R. B., Lam, M. M., Denton, M. H., Borovsky, J. E., & Green, J. C. (2011). Energetic electron precipitation during high-speed solar wind stream driven storms. *Journal of Geophysical Research: Space Physics*, *116*(A5), A05223. doi: 10.1029/2010JA016293

Millan, R. M., & Thorne, R. M. (2007). Review of radiation belt relativistic electron losses. *Journal of Atmospheric and Solar-Terrestrial Physics*, *69*, 362–377. (Received 9 May 2006; received in revised form 20 June 2006; accepted 26 June 2006; Available online 20 February 2007) doi: 10.1016/j.jastp.2006.06.018

Miyoshi, Y., & Kataoka, R. (2011). Solar cycle variations of outer radiation belt and its relationship to solar wind structure dependences. *Journal of Atmospheric and Solar-Terrestrial Physics*, *73*(10), 1324–1330. (Received 15 June 2009, Received in revised form 19 June 2010, Accepted 28 September 2010, Available online 13 October 2010)

Mourenas, D., Artemyev, A., Ma, Q., Agapitov, O., & Li, W. (2016). Fast dropouts of multi-mev electrons due to combined effects of emic and whistler mode waves. *Geophysical Research Letters*, *43*, 4155–4163. doi: 10.1002/2016GL068921

Moya, P. S., Pinto, V. A., Sibeck, D. G., Kanekal, S. G., & Baker, D. N. (2017). On the effect of geomagnetic storms on relativistic electrons in the outer radiation belt: Van allen probes observations. *Journal of Geophysical Research: Space Physics*, *122*, 11100–11108. doi: 10.1002/2017JA024735

Mursula, K., Qvick, T., Holappa, L., & Asikainen, T. (2022). Magnetic storms during the space age: Occurrence and relation to varying solar activity. *Journal of Geophysical Research: Space Physics*, *127*, e2022JA030830. (Received 8 JUL 2022, Accepted 20 NOV 2022, 1 of 27) doi: 10.1029/2022JA030830

Ni, B., Xiang, Z., Gu, X., Shprits, Y. Y., Zhou, C., Zhao, Z., . . . Zuo, P. (2016). Dynamic responses of the earth's radiation belts during periods of solar wind dynamic pressure pulse based on normalized superposed epoch analysis. *Journal of Geophysical Research: Space Physics*, *121*, 8523–8536. doi: 10.1002/2016JA023067

NOAA. (2024). *Sunspot numbers.* `https://www.swpc.noaa.gov/products/solar-cycle-progression`.

Oh, S. Y., & Yi, Y. (2011). Solar magnetic polarity dependency of geomagnetic storm seasonal occurrence. *Journal of Geophysical Research*, *116*, A06101. doi: 10.1029/2010JA016362

Onsager, T. G., Rostoker, G., Kim, H.-J., Reeves, G. D., Obara, T., Singer, H. J., & Smithtro, C. (2002). Radiation belt electron flux dropouts: Local time, radial, and particle-energy dependence. *Journal of Geophysical Research*, *107*(A11), 1382. doi: 10.1029/2001JA000187

Pinto, V. A., Zhang, X.-J., Mourenas, D., Bortnik, J., Artemyev, A. V., Lyons, L. R., & Moya, P. S. (2020). On the confinement of ultrarelativistic electron remnant belts to low l shells. *Journal of Geophysical Research: Space Physics*, *125*, e2019JA027469. Retrieved from `https://doi.org/10.1029/2019JA027469` (©2020. American Geophysical Union. All Rights Reserved.) doi: 10.1029/2019JA027469

Reeves, G. D., McAdams, K. L., Friedel, R. H. W., & O'Brien, T. P. (2003). Acceleration and loss of relativistic electrons during geomagnetic storms. *Geophysical Research Letters*, *30*(10), 1529. Retrieved from `https://doi.org/10.1029/2002GL016513` (Received 24 October 2002; revised 18 December 2002; accepted 21 March 2003; published 27 May 2003) doi: 10.1029/2002GL016513

Richardson, I. G., Cliver, E. W., & Cane, H. V. (2001). Sources of geomagnetic storms for solar minimum and maximum conditions during 1972–2000. *Geophysical Research Letters*, *28*(13), 2569–2572. Retrieved from `https://agupubs.onlinelibrary.wiley.com/doi/abs/10.1029/2001GL013052` doi: 10.1029/2001GL013052

Roederer, J. G., & Zhang, H. (2014). *Dynamics of magnetically trapped particles* (2nd ed.). New York: Springer. (Retrieved from `https://doi.org/10.1007/978-3-642-41530-2`)

Russell, C. T., & McPherron, R. L. (1973). Semiannual variation of geomagnetic activity. *Journal of Geophysical Research*, *78*, 92–108. Retrieved from `https://doi.org/10.1029/JA078i001p00092` doi: 10.1029/JA078i001p00092

Samsonov, A., Bogdanova, Y., Branduardi-Raymont, G., Safrankova, J., Nemecek, Z., & Park, J.-S. (2019). Long-term variations in solar wind parameters, magnetopause location, and geomagnetic activity over the last five solar cycles. *Journal of Geophysical Research: Space Physics*, *124*, 4049–4063. doi: 10.1029/2018JA026355

Shprits, Y. Y., Elkington, S. R., Meredith, N. P., & Subbotin, D. A. (2008). Review of modeling of losses and sources of relativistic electrons in the outer radiation belt i: Radial transport. *Journal of Atmospheric and Solar-Terrestrial Physics*, *70*, 1679–1693. doi: 10.1016/j.jastp.2008.06.008

Shprits, Y. Y., Thorne, R. M., Friedel, R., Reeves, G. D., Fennell, J., Baker, D. N., & Kanekal, S. G. (2006). Outward radial diffusion driven by losses at magnetopause. *Journal of Geophysical Research*, *111*, A11214. doi:

10.1029/2006JA011657

Summers, D., & Thorne, R. M. (2003). Relativistic electron pitch-angle scattering by electromagnetic ion cyclotron waves during geomagnetic storms. *Journal of Geophysical Research*, *108*(A4), 1143. (Correction published 14 January 2005) doi: 10.1029/2002JA009489

Torii, S., Marrocchesi, P. S., & CALET Collaboration. (2019). The calorimetric electron telescope (calet) on the international space station. *Advances in Space Research*, *64*(12), 2531–2537. (Available online 13 May 2019) doi: 10.1016/j.asr.2019.04.007

Turner, D. L., Kilpua, E. K. J., Hietala, H., Claudepierre, S. G., O'Brien, T. P., Fennell, J. F., et al. (2019). The response of earth's electron radiation belts to geomagnetic storms: Statistics from the van allen probes era including effects from different storm drivers. *Journal of Geophysical Research: Space Physics*, *124*, 1013–1034. (Retrieved from https://doi.org/10.1029/2018JA026066)

Turner, D. L., Morley, S. K., Miyoshi, Y., Ni, B., & Huang, C. L. (2012). Outer radiation belt flux dropouts: Current understanding and unresolved questions. *Geophysical Monograph Series*, *199*, 195–212. doi: 10.1029/2012GM001310

Turner, D. L., Shprits, Y., Hartinger, M., & et al. (2012). Explaining sudden losses of outer radiation belt electrons during geomagnetic storms. *Nature Physics*, *8*, 208–212. doi: 10.1038/nphys2185

Van Allen, J. A. (1959, November). The geomagnetically trapped corpuscular radiation. *Journal of Geophysical Research*, *64*(11), 1587-1594.

Vidal-Luengo, S. E., Blum, L. W., Bruno, A., Ficklin, A. W., de Nolfo, G., Guzik, T. G., … Torii, S. (2024, April 25). Characterization of relativistic electron precipitation events observed by the CALET experiment using self-organizing-maps. *Journal of Geophysical Research: Space Physics*, *129*(4), e2024JA032481. Retrieved from https://doi.org/10.1029/2024JA032481 doi: 10.1029/2024JA032481

Vidal-Luengo, S. E., Blum, L. W., Bruno, A., Guzik, T. G., de Nolfo, G., Ficklin, A. W., et al. (2024). Comparative observations of the outer belt electron fluxes and precipitated relativistic electrons. *Geophysical Research Letters*, *51*, e2024GL109673. (Received 7 APR 2024, Accepted 4 JUN 2024) doi: 10.1029/2024GL109673

Xiang, Z., Tu, W., Li, X., Ni, B., Morley, S. K., & Baker, D. N. (2017). Understanding the mechanisms of radiation belt dropouts observed by van allen probes. *Journal of Geophysical Research: Space Physics*, *122*, 9858–9879. doi: 10.1002/2017JA024487

Xiang, Z., Tu, W., Ni, B., Henderson, M. G., & Cao, X. (2018). A statistical survey of radiation belt dropouts observed by van allen probes. *Geophysical Research Letters*, *45*, 8035–8043. Retrieved from https://doi.org/10.1029/2018GL078907 doi: 10.1029/2018GL078907

Xiong, Y., Xie, L., Pu, Z., Fu, S., Chen, L., Ni, B., … Parks, G. K. (2015). Responses of relativistic electron fluxes in the outer radiation belt to geomagnetic storms. *Journal of Geophysical Research: Space Physics*, *120*, 9513–9523. doi: 10.1002/2015JA021440

Yan, Y., Yue, C., Ma, Q., Zhou, X.-Z., Zong, Q.-G., Fu, H., … Li, Y.-X. (2023). Prompt appearance of large-amplitude EMIC waves induced by solar wind dynamic pressure enhancement and the subsequent relativistic electron precipitation. *Journal of Geophysical Research: Space Physics*, *128*, n/a–n/a. Retrieved from https://doi.org/10.1029/2023JA031399 doi: 10.1029/2023JA031399

Yu, Y., Koller, J., & Morley, S. K. (2013). Quantifying the effect of magnetopause shadowing on electron radiation belt dropouts. *Annales Geophysicae*, *31*, 1929–1939. Retrieved from https://www.ann-geophys.net/31/1929/2013/ (© Author(s) 2013. CC Attribution 3.0 License.) doi: 10.5194/angeo-31-1929-2013